PHYSICAL REVIEW C VOLUME 56, NUMBER 2 AUGUST 1997

Charged-particle evaporation from hot ^{164}Yb compound nuclei and the role of ^{5}He emission

R. J. Charity, M. Korolija,* D. G. Sarantites, and L. G. Sobotka
Department of Chemistry, Washington University, St. Louis, Missouri, 63130

(Received 27 February 1997)

A systematic study of the decay properties of ^{164}Yb compound nuclei with excitation energies of 100–300 MeV was performed. The emission patterns of light charged particles detected in coincidence with evaporation residues produced in ^{64}Ni+^{100}Mo and ^{16}O+^{148}Sm reactions have been measured and compared to statistical model predictions. There is found to be significant disagreement between the experiment and the model calculations in the magnitude of the multiplicities and the peak position in the energy spectra. For deuterons and tritons, significant nonstatistical components were present at all excitation energies. The proton energy spectrum did not exhibit any entrance-channel dependence at an excitation energy of ~170 MeV. However for α particles, there is an enhancement in the spectrum at the lowest kinetic energies for the more symmetric reaction. It is suggested that the emission and subsequent decay of ^{5}He fragments, can account for a large fraction of the apparent, and often reported, decrease in the Coulomb barrier for α particle emission. [S0556-2813(97)02408-4]

PACS number(s): 25.70.Jj, 24.60.Dr

I. INTRODUCTION

The study of the decay properties of hot nuclei produced in heavy-ion collisions is an active field of investigation. For reactions which are associated with compound nucleus excitation energies of less than 300 MeV, data are routinely compared to predictions of statistical model calculations. A substantial number of studies have concluded that the peaks of the experimental charged-particle energy spectra are shifted down in energy compared to predictions for the statistical decay of spherical nuclei [1–8]. This shift has often been interpreted as a lowering of the average Coulomb barrier due to deformation or due to a large surface diffuseness. However, the interpretation of results for lighter systems [1,3] have been controversial [9,10].

Dynamical fusion models [11] predict that the initial fused object can be quite deformed and the time period required for shape equilibration can be long (10 zs). Charged-particle emission during this period will be affected by this deformation [12] and may contribute to the lowering of the Coulomb barriers [13]. The nature of the predicted fusion dynamics depends greatly on the entrance-channel mass asymmetry. Entrance channels with mass asymmetries greater than that of the Businaro-Gallone peaks in the potential-energy surface are associated with shorter fusion times and little deformation during fusion. On the other hand, those with smaller mass-asymmetries have longer fusion times, during which the fused system is more deformed. These predictions lead to a dependence of the deexcitation process on the entrance-channel mass asymmetry.

For reactions with bombarding energies near their fusion barrier, experimental investigations of the yield of energetically ‘‘expensive’’ decay products such as deuterons, tritons, and high-energy γ rays have shown dependences on the entrance channel’s mass asymmetry [12,14]. If interpreted in terms of fusion dynamics, the data imply longer time scales for the shape equilibration than is predicted. At higher bombarding energies where decay rates for light particle emission are much larger, the observation that the shape of the α particle energy spectrum is independent of entrance-channel mass asymmetry [6,8] has cast some doubts on the extent to which fusion dynamics influences the deexcitation process.

Other discrepancies between statistical model simulations and experimental data exist. Gonin *et al.* [4] report experimental charged-particle multiplicities at large excitation energies which are significantly lower than statistical model estimates. Another study found that evaporation residues were, on average, more neutron deficient than expected [15]. The extent to which charged particle multiplicities are correctly predicted at large excitation energies is clearly in need of further study.

With these considerations in mind, we have continued an investigation of the energy spectra and angular distributions of charged particles detected in coincidence with evaporation residues to study the decay of ^{164}Yb compound nuclei. In our original study [16,17], the ^{164}Yb compound nuclei were formed with an excitation energy of 54 MeV and the dominant decay modes were well described by statistical model calculations. Only the rare deuteron and triton decay channels were found to have a significant dependence on the entrance-channel mass asymmetry [12]. In the present work, the ^{64}Ni+^{100}Mo reaction is used to follow the decay properties of ^{164}Yb compound nuclei from $E^*=100$ to 280 MeV. In conjunction with this, a search for an entrance-channel dependence of the deexcitation process is made at $E^*=170$ MeV using the same set of reactions as the original study; ^{16}O+^{148}Sm and ^{64}Ni+^{100}Mo. These two reactions have mass asymmetries which straddle the Businaro-Gallone value.

In this work, we also will present an alternative explana-

---

*Present address: Rudjer Boskovic Institute, Zagreb, Republic of Croatia.

TABLE I. For each of the reactions studied in this work, the compound nucleus excitation energy is listed as well as the distance between the target and PPAC and the resulting angular acceptance of the PPAC.

Projectile	E/A (MeV)	Excitation energy (MeV)	PPAC-target distance (cm)	PPAC angular range (deg)
^{64}Ni	5.0	102	36.1	1.5−6.6
^{64}Ni	6.8	170	36.1	1.5−6.6
^{64}Ni	9.0	258	27.0	1.9−8.9
^{64}Ni	10.0	296	36.1	1.5−6.6
^{16}O	13.4	170	20.1	2.6−11.7
			16.3	3.2−16.8

TABLE II. Center angle for each Microball ring and the number of detectors per ring.

Ring	Center angle	No. of detectors
1		
2	21°	10
3	36°	12
4	52°	12
5	70°	14
6	90°	14
7		
8	135°	10
9	159°	6

tion of the apparent reduction in the Coulomb barriers observed in the energy spectra of α particles. The emission of the particle-unstable ^{5}He ground state will be shown in statistical model calculations to account for a large fraction of the low-energy α particles observed at large excitation energies.

The experimental apparatus used for the detection of evaporation residues and light charged particles is discussed in Sec. II. The results are presented and compared to standard statistical model predictions in Sec. III. A discussion of the disagreement between the experimental results and the statistical model calculations and an examination of some possible explanations, including ^{5}He emission, can be found in Sec. IV. Finally in Sec. V, the conclusions of this work are summarized and suggestions for the directions of further studies are presented.

II. EXPERIMENTAL METHOD

The decay of the compound nucleus ^{164}Yb was studied by bombarding beams of ^{64}Ni and ^{16}O projectiles on targets of ^{100}Mo (0.30 mg/cm^2) and ^{148}Sm (0.86 mg/cm^2), respectively. The nickel beams of bombarding energies $E/A=5.0$, 6.8, 9.0, and 10.0 MeV and the oxygen beams of $E/A=13.4$ MeV were extracted from the ALTAS accelerator facility at the Argonne National Laboratory. The beams were bunched with pulse widths of less than 1 ns.

Evaporation residues were detected in an annular parallel plate avalanche counter (PPAC) centered at zero degrees with its anode subdivided into six concentric rings. The distance between the counter and the target was adjusted, depending on the reaction, to obtain an optimum sampling of the residue angular distribution. The maximum and minimum angles covered by the PPAC are listed in Table I for each reaction. Evaporation residues were separated from other reaction products by measurements of their energy loss in the PPAC gas volume and the time of flight to the PPAC. Absolute evaporation residue cross sections were determined from the beam charge collected in a Faraday cup.

Light charged particles evaporated from the compound nuclei were detected with the Microball CsI(Tl) array (Reaction version) [18]. The first ring of the Microball was removed to avoid shadowing the PPAC and the seventh ring was not operational in this experiment. Therefore, light charged particles were detected in seven rings of detectors covering the full angular range from 14° to 171° except for a break from 100° to 123°. The central angle of each ring is listed in Table II. In order to eliminate the large counting rate due to elastically scattered projectiles, Pb absorbers were placed in front of the CsI(Tl) crystals in rings 2 and 3 with thicknesses of ~133 and 74 mg/cm^2, respectively. For all other detectors, 5 mg/cm^2 Sn-Pb absorbers were used to reduce the counting rate from δ electrons and x rays.

The light output of the CsI(Tl) crystals was assumed to vary linearly with particle energy for the hydrogen isotopes. The absolute calibrations of the light output of all detectors were obtained from the energy at which these fragments punched through the CsI(Tl) crystals. This energy was calculated from the tables of Janni [19]. For α particles, the functional dependence of the light output on energy was taken from Ref. [18], with coefficients modified in order to fit data points obtained from a ^{232}U α source and from elastically scattered α particle beams of energies 21, 35, and 42 MeV.

III. RESULTS

The energy spectra and angular distributions of charged particles and evaporation residues will be presented in this section. As they are presented they will be compared to predictions of standard statistical model calculations. By standard we mean, calculations typically used by other authors when comparing to data including only n, p, d, t, ^{3}He, α, γ-ray, and symmetric fission decay channels. In this case, the calculations were performed with the statistical model code GEMINI [20,21]. The level density parameter was obtained from Lestone's temperature-dependent parametrization [22] modified to account for the fading influence of the ground-state shell corrections [23]. Transmission coefficients were obtained from the incoming-wave boundary-condition calculations [24] using real nuclear potential obtained from global optical model fits [25–29].

Particle emission angles were obtained from a quantum mechanical treatment, the projection of the initial compound nucleus spin along the beam axis was assumed to be zero ($m=0$). The projections of the spins of all particles and their orbital angular momenta were chosen using Clebsch-Gordan coefficients. The θ angle of an emitted particle with angular momentum quantum numbers m and ℓ, was taken to have

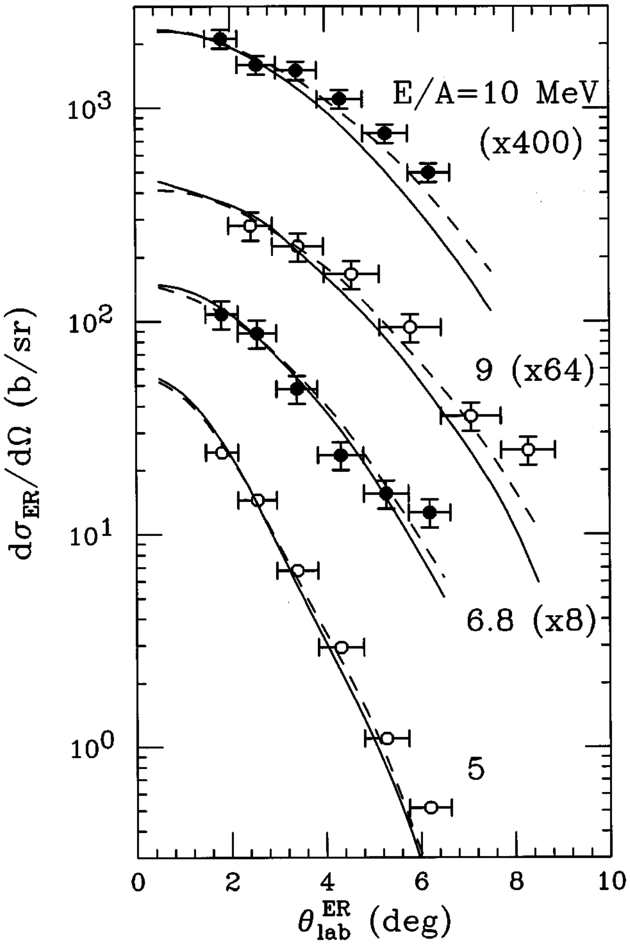

FIG. 1. Experimental evaporation residue angular distributions obtained in the ^{64}Ni+^{100}Mo reactions are compared to the statistical model predictions indicated by the curves. The dashed curves were obtained from calculations including ^{5}He emission while, for the solid curves, this fragment was excluded. For clarity, the results for the higher bombarding energies have been scaled by the indicated factors.

the distribution $|P_\ell^{|m|}[\cos(\theta)]|^2\sin(\theta)$, where P_ℓ^m is the associated Legendre polynomial of the first kind. Finally to take into account the experimental biases, only simulated events which pass a ''detector filter'' were used for comparison with experimental data.

A. ^{64}Ni+^{100}Mo

1. Evaporation residues

Angular distributions of evaporation residues obtained from the four ^{64}Ni-induced reactions are shown in Fig. 1. The angular ranges subtended by each annular ring of the PPAC are indicated by the horizontal error bars. The vertical error bars show only the statistical uncertainty. The systematic uncertainty due to absolute normalization of the Faraday cup and to the estimate of the average residue charge state [30] is ±25%. The standard statistical model predictions, indicated by the solid curves, have been normalized to the yield in the first two rings. They do a reasonable job of reproducing the shape of the angular distributions. However, for the $E/A=9.0$ and 10.0 MeV reactions, the predicted distributions are slightly narrower than the experimental data.

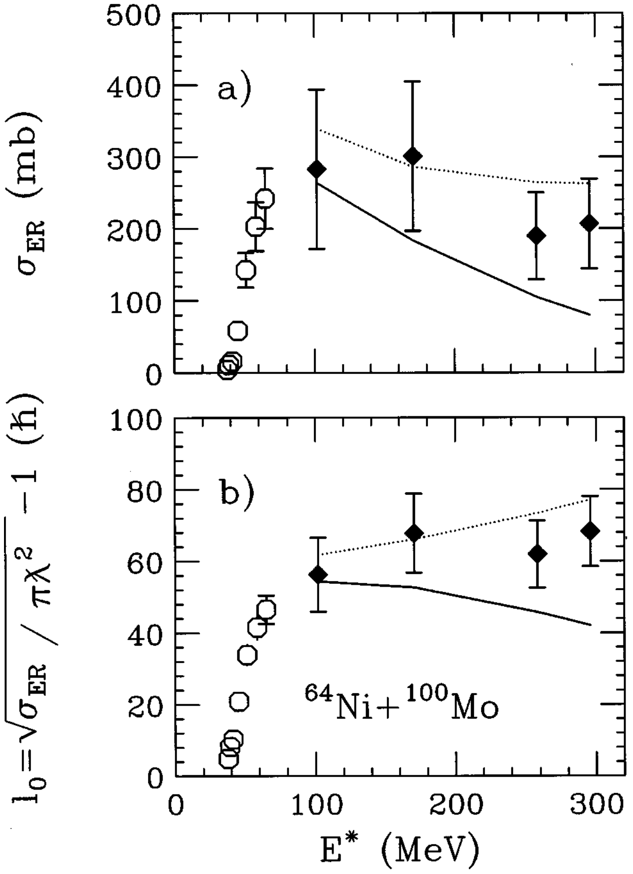

FIG. 2. (a) Experimental evaporation residue excitation functions measured for the ^{64}Ni+^{100}Mo reactions in this work (solid symbols) and from Ref. [33] (open symbols). (b) Values of the maximum partial waves contributing to evaporation residue production are plotted as a function of the compound nucleus excitation energy. The two curves indicate statistical model predictions obtained with $a_f/a_n=1.00$ (dotted curve) and 1.06 (solid curve).

The effect of multiple scattering of the evaporation residues in the target was investigated. The magnitude of the scattering was estimated from Refs. [31,32] and was found to have little effect on the shapes of the angular distributions. The predictions in Fig. 1 include the predicted smearing due to this effect.

Evaporation residue cross sections were obtained by integrating the angular distributions. They are plotted as solid points in Fig. 2(a) as a function of the excitation energy of the compound nucleus. The error bars contain the systematic uncertainties mentioned previously plus the uncertainty associated with extrapolating the angular distributions to zero degrees. This uncertainty is largest for the $E/A=5.0$ MeV reaction where the GEMINI predictions suggest that 34% of the residues passed inside of the inner edge of the PPAC and thus were not detected. This bias in selecting the evaporation residues will have consequences when discussing the measured angular distributions of α particles in Sec. III A 4.

Also plotted in Fig. 2(a) are ^{64}Ni+^{100}Mo evaporation residue cross sections measured by Rehm *et al.* [33] for bombarding energies located near the Coulomb barrier. In contrast to these lower energy results, the residue cross sections at the higher energies are no longer rising rapidly, but decrease slowly with increasing bombarding energy. This behavior is expected when the partial waves associated with evaporation residues are limited by competition with equilibrium fission or nonequilibrium exit channels such as fast fission or deep inelastic scattering. If the maximum partial waves associated with residue formation saturate at a value ℓ_0, then the residue cross section is approximately

$$\sigma_{\mathrm{ER}}=\pi \lambda\!\!\!^{-2}(\ell_0+1)^2, \tag{1}$$

assuming a sharp transition from residue formation to fission. The residue cross section therefore decreases with increasing bombarding energy due to the $1/E_{\mathrm{c.m.}}$ energy dependence of the quantity $\lambda\!\!\!^{-2}$. The quantity ℓ_0 is plotted in Fig. 2(b) and we see that it saturates at $\sim 65\hbar$.

In reality ℓ_0 may only approximately saturate. This is illustrated by the curves in Fig. 2 which were obtained from two statistical model calculations, one where a_f/a_n, the ratio of level density parameters at the saddle point and at the equilibrium deformation, is unity (dotted curve) and the other is for $a_f/a_n=1.06$ (solid curve). Neither of these two curves is exactly flat, however, and more importantly, they indicate that the data are consistent with intermediate values of a_f/a_n. This result may suggest that competition with equilibrium fission is limiting ℓ_0. Alternatively one may assume that fusion reactions are restricted to ℓ waves for which the initial fission barrier is larger than the initial temperature (a condition necessary for strict application of the transition state theory of statistical fission). Using Sierk's fission barriers [34] the limiting value of ℓ_0 for fusion reactions from this condition is $\sim 70\ \hbar$ which is also consistent with the data. However, the above condition may be too simplistic especially if the fusion time is long and significant angular momentum is removed by particle evaporation during this phase. As an alternative condition, we have assumed that fusion is still possible if after some delay time associated with the fusion dynamics, the angular momentum-dependent fission barrier becomes larger than the temperature of the system. Within this scenario, GEMINI simulations predict that delay times of 20 zs or greater would generate an unobserved enhancement in the residue yield at the two highest bombarding energies. The angular momentum loss during the delay time was calculated both with a spherical composite system and with a highly deformed prolate shape with a three to one ratio of major to minor axes. The lack of an enhancement in the residue cross section suggests that for ℓ waves of magnitude $70\hbar$ or greater, either the delay period is too small to allow for the development of a pocket in the potential energy surface or that the collision dynamics do not allow the system to fall into this pocket.

The saturation in ℓ_0 is important as it implies that the partial-wave distributions associated with evaporation residues are approximately equivalent for the four bombarding energies. Therefore, any bombarding energy dependence of the charged-particle multiplicities and angular distributions are associated with either the evolution of the excitation energy or fusion dynamics, but not with differences in the spin distributions. The two values of a_f/a_n were chosen to span the uncertainty associated with the experimental values of σ_{ER} or ℓ_0. As such, calculations with these two values of a_f/a_n are useful to determine how the uncertainty in the partial-wave distributions affects the predicted charged particle multiplicities and angular distributions. In general the effects are small, larger ℓ waves are predicted to have increased α particle emission and decreased p,d,t emission. The predicted p,d,t, and α multiplicities differ by at most 9% for the two values of a_f/a_n. In the following sections, only GEMINI predictions with $a_f/a_n=1.00$ will be presented, however, the general conclusions drawn from comparisons of the statistical model predictions with the data are identical for $a_f/a_n=1.06$. The largest effect of changing a_f/a_n is on the α particle angular distributions which will be discussed in Sec. III A 4.

2. Proton evaporation

The measured angular distributions and energy spectra for charged particles measured in coincidence with evaporation residues were transformed event-by-event into the reaction center-of-mass frame (c.m.). Because of the large compound nucleus velocity, of those particles emitted backwards, only those with the largest emission velocities have laboratory energies sufficient to exceed the particle identification threshold. Therefore, for rings 8 and 9 of the Microball (the two most backward rings) only the exponential tails of energy spectra were measured.

For protons, the associated center-of-mass energy spectra obtained with each Microball ring are very similar in shape and magnitude. To highlight the similarity in shape, the energy spectra for each ring were scaled to the yield in ring 3. These spectra are displayed in Fig. 3 for the four bombarding energies. The degree to which the spectra are similar can be gauged by the overlap of all the curves. Note for rings 8 and 9 where only the exponential tails of the spectra were above threshold, one can only conclude that the slope of these tails are consistent with those from the other rings.

A detailed examination of the spectra reveals that the largest deviations between rings occurs for the very high-energy tails of the $E/A=9.0$ and 10.0 MeV data. Here, the forward-angle rings show slightly harder tails indicating the onset of pre-equilibrium emission. This effect will be discussed later, but it should be stressed that these angle-dependent deviations are very small and overall the shape of the proton energy spectra are almost independent of angle.

The magnitude of the differential proton multiplicity also shows little angular dependence. The proton angular distributions are displayed in Fig. 4. The differential proton multiplicity for each ring, obtained by the integrating the associated energy spectra, are plotted versus the average proton center-of-mass angle. For rings 8 and 9, the shapes of the proton spectra determined with the other rings were used to extrapolate below the low-energy threshold. Within the experimental uncertainties, these center-of-mass angular distributions are isotropic, consistent with statistical emission. From the average values of $dm/d\Omega$ (indicated by the lines in Fig. 4), the proton multiplicities, plotted in Fig. 5, were extracted. The GEMINI predictions, which are indicated by the curve in this figure, follow an excitation energy dependence which is similar to that exhibited by the experimental multiplicities. However, these predicted multiplicities are consistently 40–60 % larger than the experimental values.

The GEMINI simulations predict that the proton angular distributions are isotropic, as was found experimentally. In Fig. 6, the simulated energy spectra are compared to the experimental results obtained from ring 5, for which any

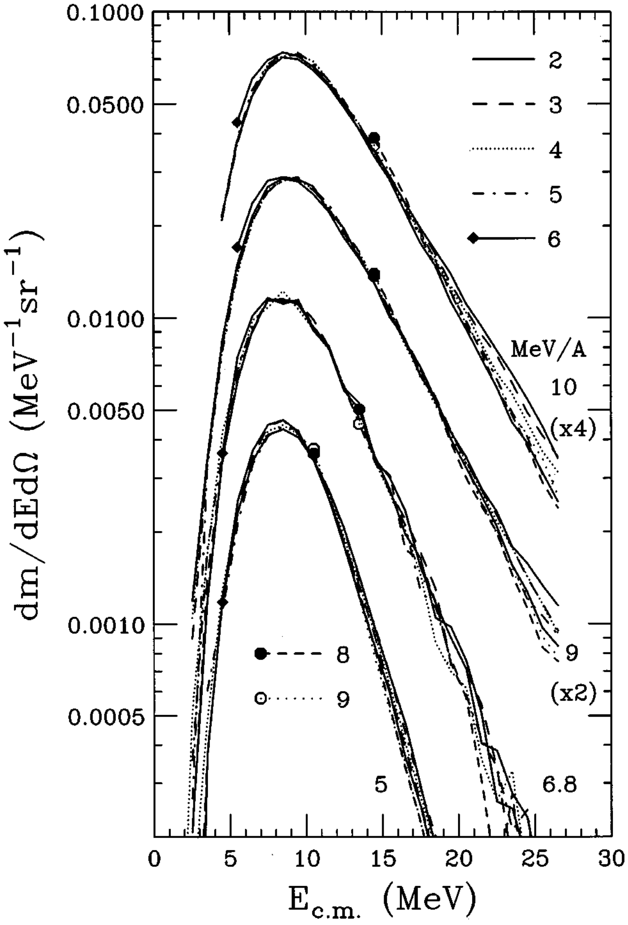

FIG. 3. Experimental proton energy spectra obtained from the ^{64}Ni+^{100}Mo reactions for each of the indicated Microball rings and bombarding energies. To highlight the similarity in shapes, the curves have been normalized to the yield measured for ring 3 at each bombarding energy. Symbols are used for rings 6, 7, and 8 to indicate the values of the low-energy threshold. For clarity, the results from the higher bombarding energies have been scaled by the indicated factors.

pre-equilibrium component is negligible. At all four bombarding energies, the predicted spectra are in agreement with the data only at the very lowest proton energies (5–8 MeV), otherwise the calculated differential multiplicities are consistently larger. As a consequence, the simulated peak yield and the average proton energy are ~1 MeV larger than the experimental values. However, the simulations do reproduce the slope of the exponential tail at all four bombarding energies.

3. Deuteron and triton emission

Deuterons and tritons detected in coincidence with evaporation residues, show features which are even more difficult to reconcile with statistical model predictions. In fact, they clearly have a relatively large nonstatistical component. This is illustrated in Fig. 7 where energy spectra for the three hydrogen isotopes detected in the $E/A = 9.0$ MeV reaction are shown for rings 2 and 9 (the most forward and most backward Microball rings). For protons, one finds that the high-energy tails are consistent in slope and magnitude, except at the very highest proton energies where a small nonstatistical component enhances the forward angles.

In contrast, for deuterons and tritons one finds the exponential tails in the two rings differ in magnitude by a factor of ~2. Therefore, these exponential tails have center-of-mass angular distributions which are forward peaked and inconsistent with the expected behavior for statistical emission, i.e., symmetry about $\theta_{\mathrm{c.m.}} = 90°$. Also shown in Fig. 7 are energy spectra predicted by the GEMINI calculations. In contrast to the case for protons, the experimental spectra, for the forward angles at least, exhibit much harder exponential tails than predicted. In fact, the slopes of the tails are larger than that predicted for *first chance* emission. Clearly, high-energy deuteron and triton emission is dominated by nonstatistical processes. Even more surprisingly, these observations are true at all four bombarding energies, including the lowest. In Fig. 8, the deuteron energy spectra, determined from rings 2 and 9, are shown as a function of bombarding energy. The forward peaked angular distributions of the high-energy tail

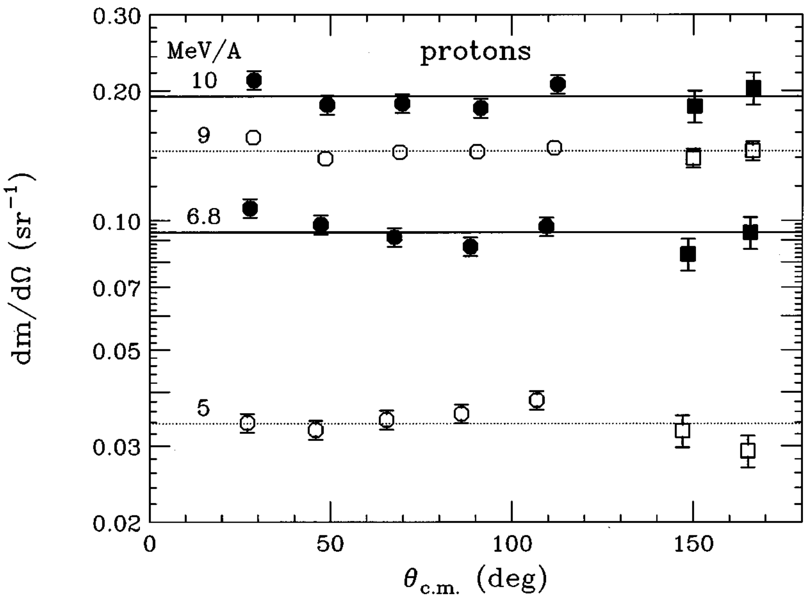

FIG. 4. Experimental angular distributions measured for protons in the ^{64}Ni+^{100}Mo reactions for the four indicated bombarding energies. The results depicted by the square symbols were obtained by using the shapes of the forward angle spectra to extrapolate below the low-energy threshold. The curves indicate the mean values of these differential multiplicities.

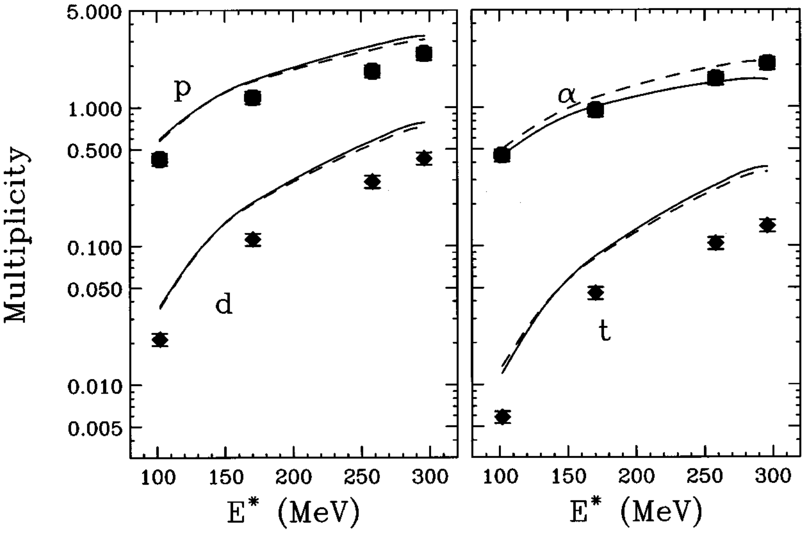

FIG. 5. Experimental multiplicities of protons, deuterons, and tritons measured in the ^{64}Ni+^{100}Mo reactions as a function of compound nucleus excitation energy. The curves indicate the statistical model predictions obtained by including (dashed curve) and excluding (solid curve) ^{5}He emission.

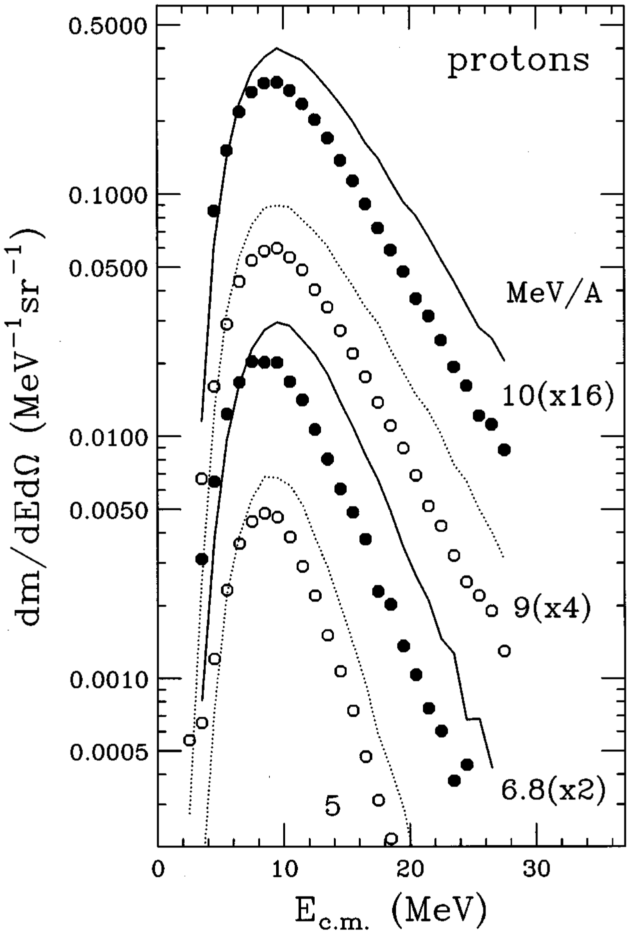

FIG. 6. Comparison of experiment proton energy spectra measured with ring 5 of the Microball to standard statistical model predictions for the ^{64}Ni+^{100}Mo reactions. For clarity, the results for the higher bombarding energies have been scaled by the indicated factors.

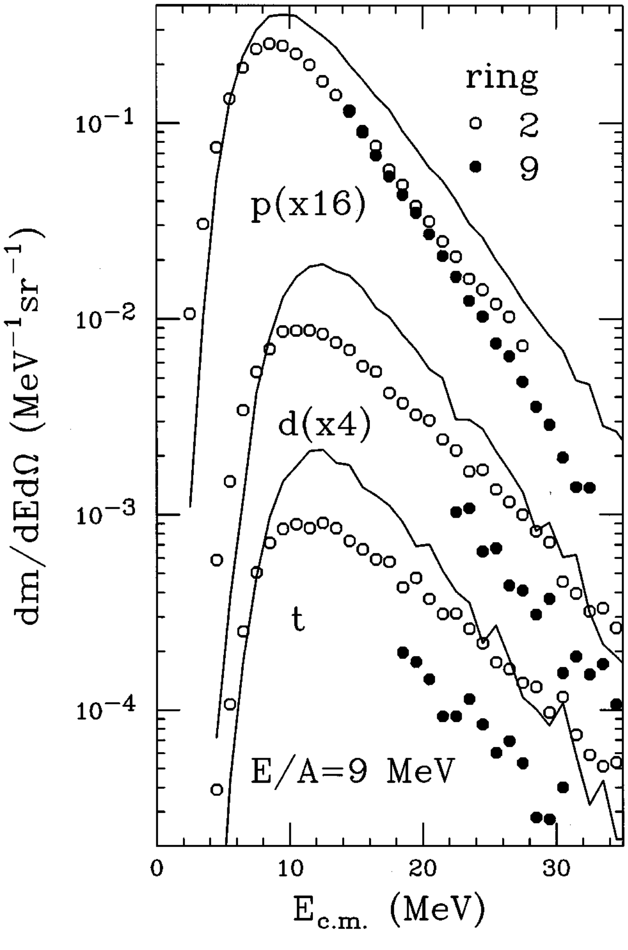

FIG. 7. Experiment energy spectra measured with rings 2 and 9 of the Microball obtained for protons, deuterons, and tritons in the $E/A=9.0$ MeV ^{64}Ni+^{100}Mo reaction. The curves indicate the results obtained from statistical model simulations. For clarity, the results for deuterons and protons have been scaled by the indicated factors.

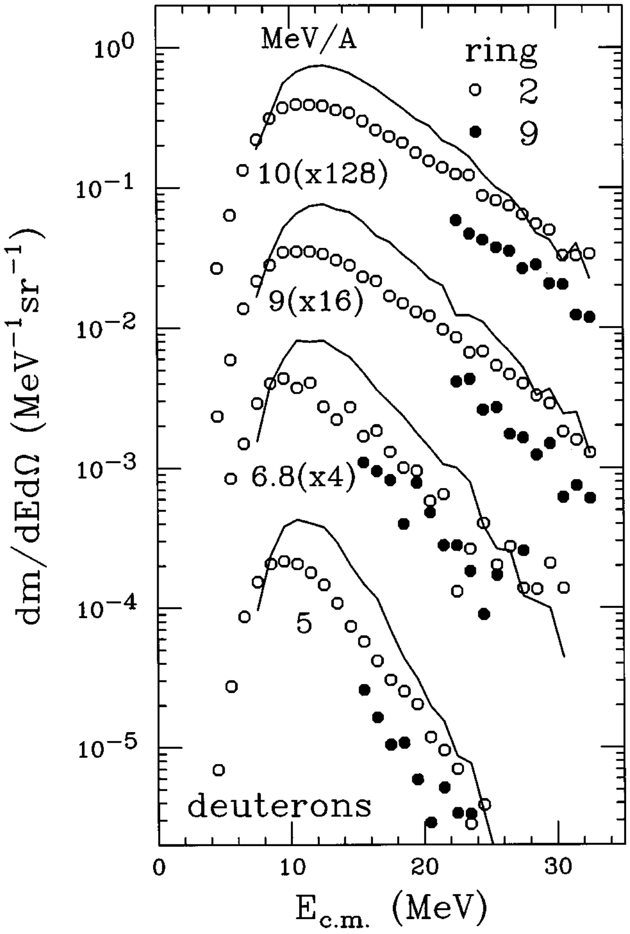

FIG. 8. Experimental deuteron energy spectra measured in rings 2 and 9 of the Microball for the ^{64}Ni+^{100}Mo reactions. For clarity, the results for the higher bombarding energies have been scaled by the indicated factors. The curves show the predictions of the statistical model calculations.

and its much harder slope, relative to the statistical model predictions, are clearly present even at the lowest bombarding energy.

To estimate the total deuteron and triton multiplicities, two approaches were followed. First for an upper limit, one can assume that the dominant lower energy deuterons and tritons are essentially all due to statistical emission. In that case, their angular distribution should be symmetric about $\theta_{c.m.}=90°$. The differential multiplicities from rings 2 to 6, where the complete energy spectra were measured, were therefore fit with the sum of zeroth- and second-order Legendre polynomials which have the appropriate symmetry. For the lower limit, it was assumed that the shape of the energy spectra is independent of angle. The shapes of forward angle spectra were then used to extrapolate below the low-energy threshold in rings 8 and 9. The resulting forward peaked angular distributions were then fit with the sum of zeroth-, first-, and second-order Legendre polynomials.

The final angular distributions and the two fits are displayed in Figs. 9 and 10 for deuterons and tritons, respectively. The differential multiplicities, depicted by the square symbols, were obtained from the extrapolation procedure and were only used in the second fit. The two fits produce quite different results at $\theta_{c.m.}=180°$, however, when integrating the total multiplicity this difference turns out to be of minor importance as the differential multiplicities are weighted by $\sin(\theta_{c.m.})$ and the total multiplicities differ by no more than 10%. Note that the angular distributions obtained for $E/A=5.0$ MeV are slightly peaked at $\theta_{c.m.}=90°$. This is a consequence of the bias introduced by the range of evaporation residue angles sampled by the PPAC. This bias will be discussed further in the next section.

The deuteron and triton multiplicities are plotted as a function of excitation energy in Fig. 5. As the magnitude of the statistical component could not be extracted, these data also represent maximum limits for this quantity. In any case, the plotted data are a factor of 2 or 3 lower than the GEMINI

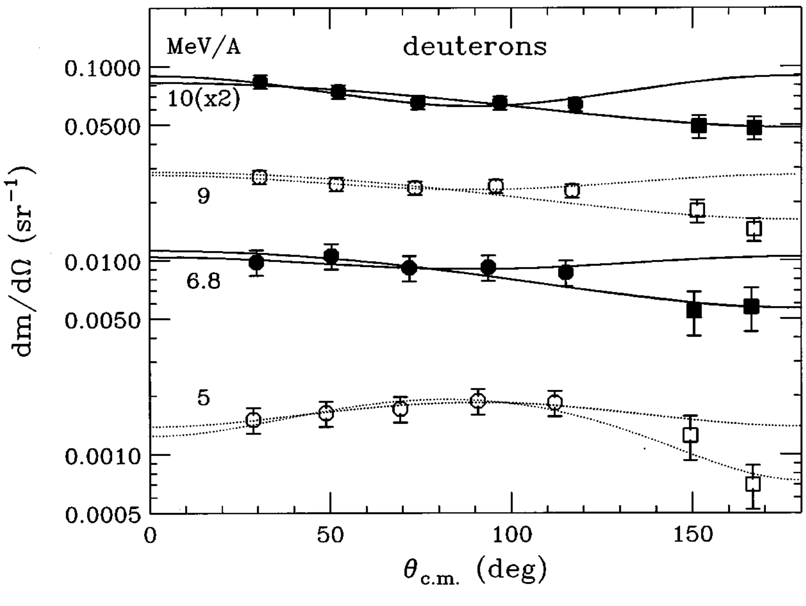

FIG. 9. Experimental deuteron angular distributions measured in the ^{64}Ni+^{100}Mo reactions for the indicated bombarding energies. The results depicted by the square symbols were obtained by using the shapes of the forward angle spectra to extrapolate below the low-energy threshold. The curves show fits to the angular distributions obtained with and without the extrapolated data points (see text).

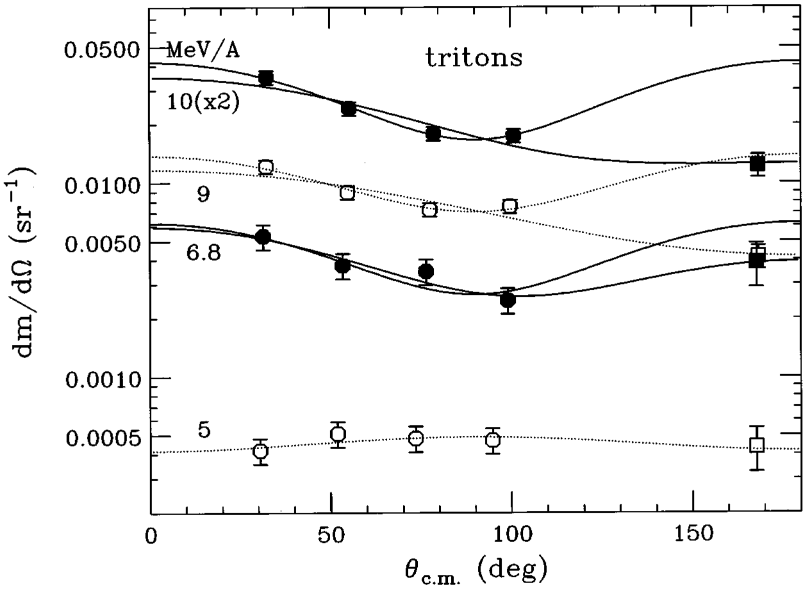

FIG. 10. Experimental triton angular distributions from the ^{64}Ni+^{100}Mo reactions. See caption of Fig. 9 for details.

predictions. However as with the protons, the relative excitation energy dependence is correctly calculated.

4. α particle evaporation

α particles, because their mass is greater and their Coulomb barrier is larger, induce a more substantial recoil motion to the decaying system than do the other charged particles. As such they have a much larger influence on the final evaporation residue angle and hence there emission patterns are much more biased when this range of angles is restricted by the detector acceptance. Care was taken to include this bias in the statistical model simulations before comparing to the data.

The measured (data points) center-of-mass energy spectra and the results from the standard calculation (solid curve) are displayed in Fig. 11 for α particles detected in ring 5 ($\theta_{\mathrm{c.m.}} \sim 90°$). As with the protons, the simulations reproduce the slope of the exponential tail. However, unlike the protons, the experimental magnitude of the tail is approximately reproduced in the simulations. For $E/A = 5.0$ MeV, the statistical model predictions reproduce both the low- and high-energy regions. However, as the bombarding energy increases, the GEMINI calculations increasingly underpredict the low-energy region and, relative to the experimental value, the position of the peak is shifted up higher in energy.

The α particle angular distributions are displayed in Fig. 12. As for the other particles, the shapes of the energy spectra measured at forward angles were used to extrapolate past the low-energy threshold in rings 8 and 9. The resulting angular distributions are approximately symmetric about $\theta_{\mathrm{c.m.}} = 90°$ and are well fit with a combination of zeroth- and second-order Legendre polynomials (see figure). Therefore they show no evidence of any substantial nonequilibrium component. The total multiplicities are also plotted as a function of excitation energy in Fig. 5. Unlike the other charged particles, the magnitude of these experimental multiplicities are in fair agreement with the standard statistical model calculations.

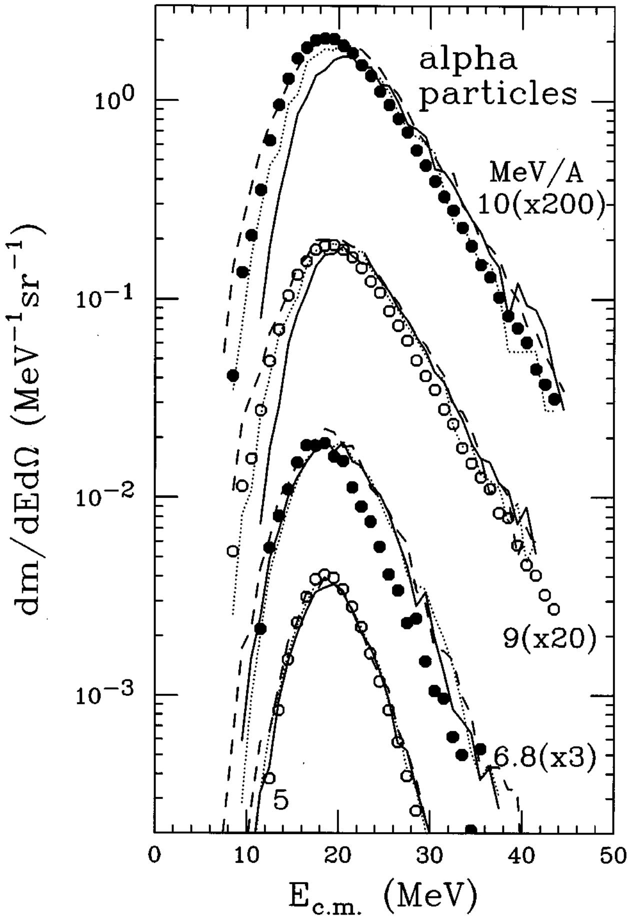

FIG. 11. Experimental α particle energy spectra obtained from ring 5 of the Microball in the indicated ^{64}Ni+^{100}Mo reactions. The curves show the predictions of statistical model calculations. The solid curves were obtained when only the evaporation of particle-stable fragments was considered in the GEMINI code. For the other curves (dotted and dashed) the evaporation of the particle-unstable ^{5}He ground state was also included in the statistical model calculations. The dashed curve is associated with the lower ^{5}He Coulomb barrier (see text).

The bias introduced by the selected range of residue angles is largest for $E/A = 5.0$ MeV. To explore this bias, the

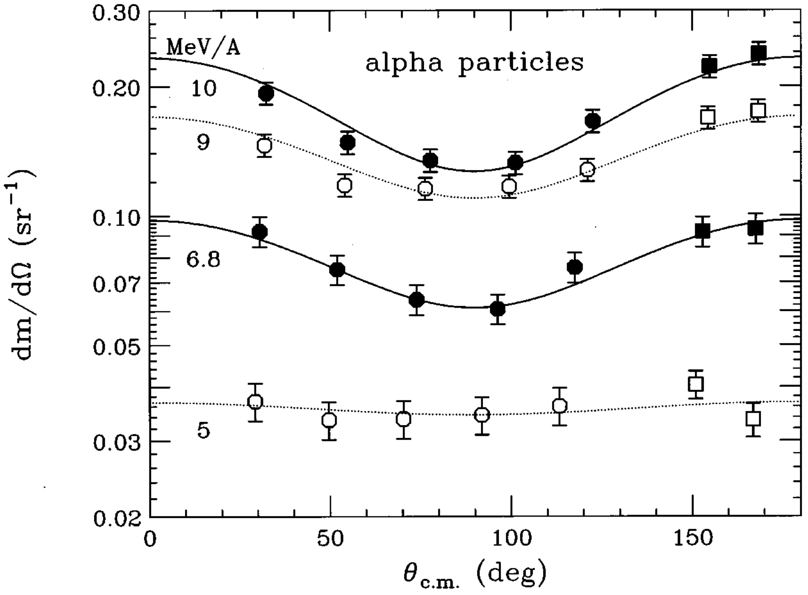

FIG. 12. Experimental α particle angular distributions measured in the indicated ^{64}Ni+^{100}Mo reactions. The results depicted by the square symbols were obtained by using the shapes of the forward angle spectra to extrapolate below the low-energy threshold. The curves are fits used to determine the total multiplicity.

angular distributions, gated on evaporation residue angle ($\theta_{\rm lab}^{\rm ER}$), are plotted in Fig. 13. The distributions show a rapid change in shape and magnitude as $\theta_{\rm lab}^{\rm ER}$ increases. This behavior is readily understood: to obtain the largest residue angles, multiple α particle emission is required and of course these are emitted at $\theta_{\rm c.m.}\sim 90°$ (collinearly). Hence the angular distributions are peaked near $\theta_{\rm c.m.}=90°$. For the smallest residue angles, α particle emission at $\theta_{\rm c.m.}\sim 90°$ must clearly be suppressed and the angular distributions must display a minimum near $\theta_{\rm c.m.}=90°$.

To quantify this effect, the ratio $R_{9/5}$ of the differential multiplicities from rings 9 and 5 is determined. This is approximately the ratio of the angular distributions at $\theta_{\rm c.m.}=180$ and 90°. These ratios are plotted as a function of residue angle in Fig. 14 for the four bombarding energies. For $E/A=5.0$ MeV, it was predicted that approximately 34% (Sec. III A 1) of residues passed inside the inner edge of the PPAC and were not detected. From the experimental dependence of $R_{9/5}$ on $\theta_{\rm lab}^{\rm ER}$, one expects these evaporation residues to be associated with very large values of $R_{9/5}$. The unbiased angular distribution will therefore have a much more pronounced minimum at $\theta_{\rm c.m.}=90°$ than is evident from the present work. The effect is smaller for the other bombarding energies as the dependence of $R_{9/5}$ on $\theta_{\rm lab}^{\rm ER}$ is not as strong and the fraction of the residues which pass inside the inner edge of the PPAC is expected to be reduced by a factor of 2 or more.

The experimental bias also affects the measured multiplicities. Figure 15 shows the dependence of the experimental α particle and proton multiplicities on the residue angle. For the lowest bombarding energy, the α particle multiplicity decreases rapidly as $\theta_{\rm lab}^{\rm ER}$ decreases. The range of residue angles accepted by the PPAC therefore selects out events with larger α particle multiplicities. In the simulation this bias results in a 30% increase in the average multiplicity for $E/A=5.0$ MeV. The dependence of the multiplicities on $\theta_{\rm lab}^{\rm ER}$ is much smaller for the other bombarding energies and so this effect should be reduced. In these cases the simula-

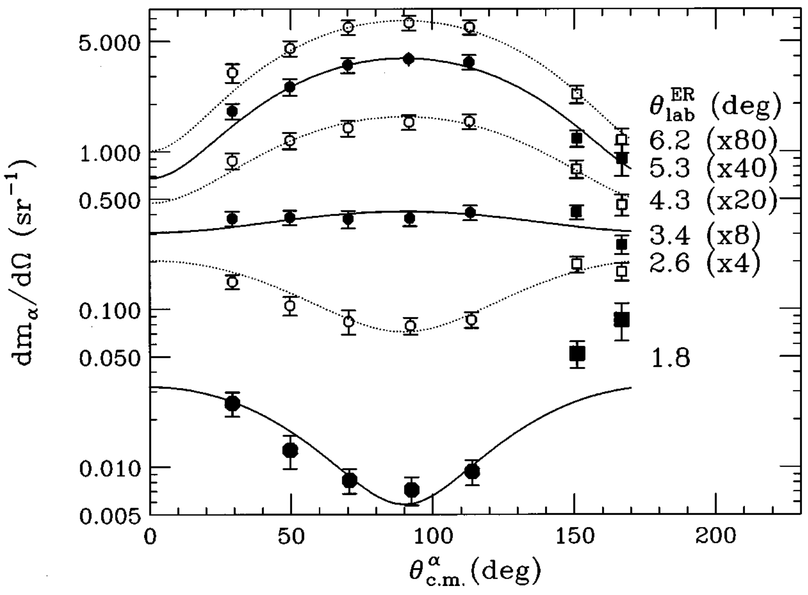

FIG. 13. Experimental α particle angular distributions obtained from the $E/A=5.0$ MeV ^{64}Ni+^{100}Mo reaction gated on the indicated evaporation residue detection angles. The curves show fits to these data used to determine the total multiplicity. For clarity, the curves have been scaled by the indicated factors.

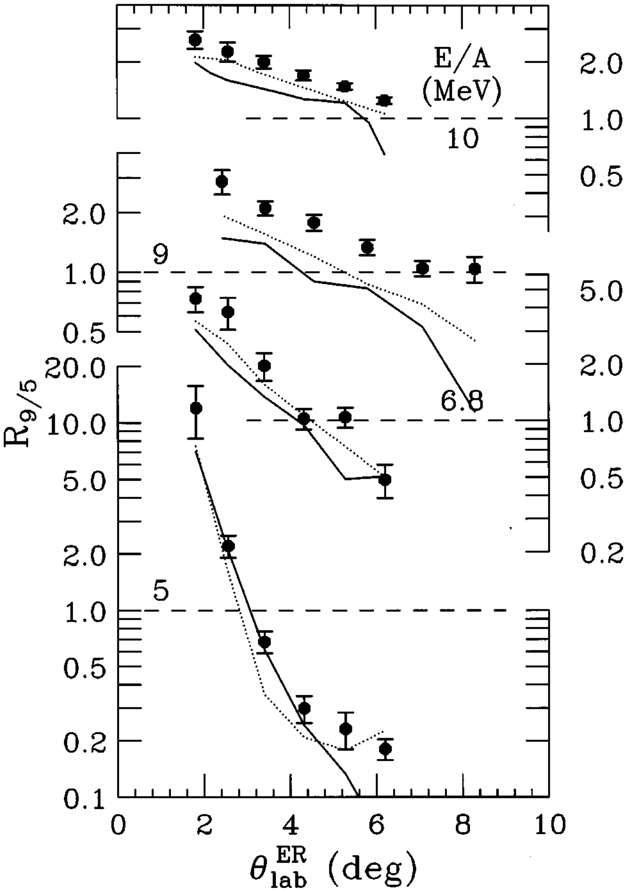

FIG. 14. Experimental ratios of the differential α particle multiplicities measured in rings 9 and 5 of the Microball plotted as a function of the angle at which the evaporation residue was detected. The solid and dotted curves show the results of statistical model calculations obtained with a_f/a_n=1.06 and 1.00, respectively.

tions predict, at most, a 4% increase in the average detected multiplicities relative to the unbiased results. The bias has a negligible influence for the proton at all bombarding energies. Note, the GEMINI simulation indicated by the curves in Fig. 15 reproduce the $\theta_{\rm lab}^{\rm ER}$ dependence of the experimental multiplicities reasonably well, though as noted in Sec. III A 2, the magnitude of the proton multiplicity is consistently overpredicted by the simulations.

The GEMINI calculations approximately reproduce the shapes of the measured angular distributions. The predicted values of $R_{9/5}$ are compared to the experimental results in Fig. 14. The predictions show some sensitivity to the value of the maximum partial wave (ℓ_0) which contributes to residue formation (see Sec. III A 1). Results obtained with a_f/a_n=1.00 and 1.06 are indicated by the dotted and solid curves, respectively. The former of these is associated with the larger ℓ_0 values and is in better agreement with the experimental data. Inclusion of even higher partial waves would further improve the agreement at the largest bombarding energies. Both calculations give approximately the correct dependence of $R_{9/5}$ on $\theta_{\rm lab}^{\rm ER}$.

B. ^{16}O+^{148}Sm

For the oxygen-induced reaction, because of the larger beam velocity, incomplete fusion processes become more important. An examination of the energy spectra of all charged particles detected in coincidence with evaporation residues reveals a strong nonstatistical component at the forward angles, especially for α particles. Therefore in this paper only the spectra obtained from rings 8 and 9, the most backwards rings of the Microball, will be presented.

1. Evaporation residues

Before examining the energy spectra, it is important to determine the degree of fusion associated with these events. The velocity of the evaporation residues were measured at two PPAC-target distances (16 and 20 cm) to check for any large systematic errors. Absolute time-of-flight measurements were obtained using elastic scattering to determine the time zero. The time zero is expected to be similar for residues and elastically scattered projectiles as they both produce signals of similar pulse height in the PPAC, i.e., there are no walk corrections. In calculating the systematic uncertainty, the error in determining the time zero is assumed to

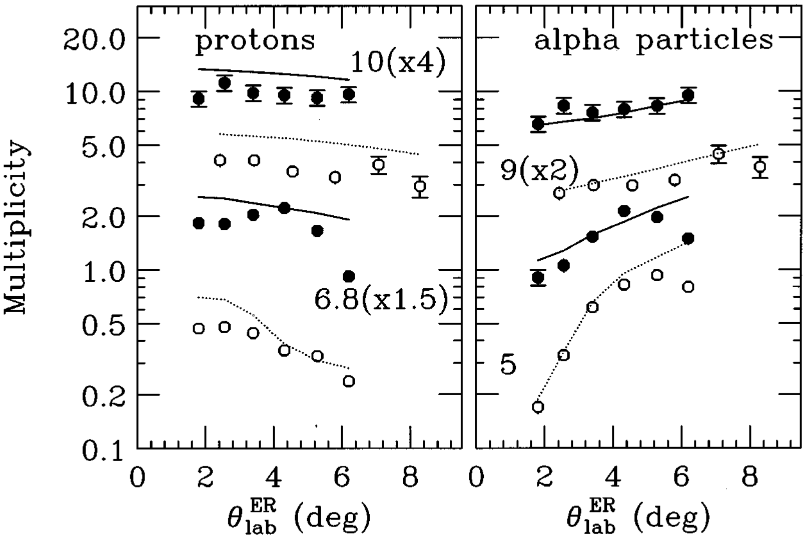

FIG. 15. Average multiplicities of proton and α particles measured as a function of evaporation residue detection angle for the indicated ^{64}Ni+^{100}Mo reactions. For clarity, the results from the higher bombarding energies have been scaled by the indicated factors.

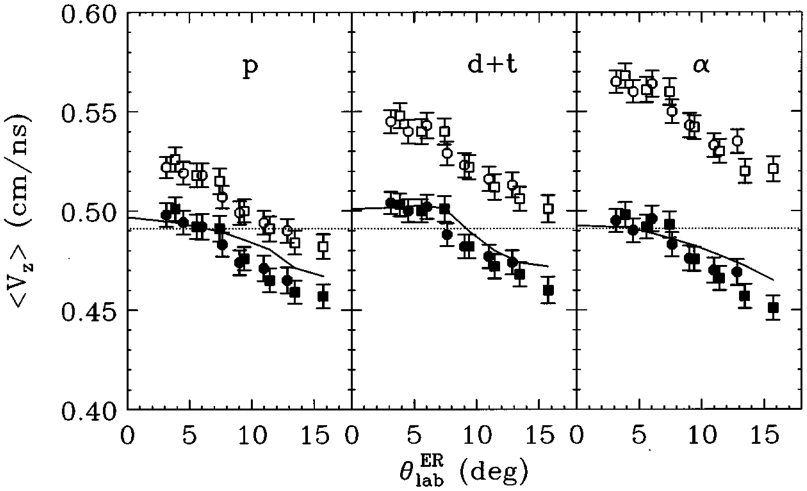

FIG. 16. Experimental average evaporation residue (open symbols) and compound nucleus (solid symbols) velocity components along the beam axis measured in the ^{16}O+^{148}Sm reaction. The dotted lines indicate the reaction center-of-mass velocity and the solid curves show the predictions of the GEMINI simulations. The results are shown when either a proton, a heavier hydrogen isotope, or an α particle is detected in rings 8 and 9, the most backward Microball rings.

be less than 2 ns. Corrections for the average energy loss in the thick Sm target were obtained from Ref. [31].

The average component of the residue velocity along the beam axis is plotted in Fig. 16 (open data points) as a function of $\theta_{\rm lab}^{\rm ER}$ when either a proton, a heavier hydrogen isotope, or an α particle is detected in rings 8 or 9. The results obtained with the target-PPAC separations of 20 and 16 cm are indicated by the circular and square data points, respectively. These two sets of measurements are in very good agreement, well within the 0.024 cm/ns systematic uncertainty. Most of the measured residue velocities are greater than the center-of-mass velocity for the reaction indicated by the dotted line. The systematic increase in this velocity with the mass of the coincident light particle, suggests that this is a bias due to the recoil motions imparted when these coincident particles were emitted backwards. Therefore to obtain the initial velocities of the fused systems, these recoil effects must be subtracted. The solid data points show the results of an event-by-event recoil correction. They no longer show any dependence on the charged-particle mass and are consistent with the center-of-mass velocity for all but the largest values of $\theta_{\rm lab}^{\rm ER}$. The GEMINI predictions, shown by the solid curves, indicate that this $\theta_{\rm lab}^{\rm ER}$ dependence is expected. From the ratio of the recoil-corrected data to the GEMINI predictions, the average velocity of the fused system was determined to be 0.98±0.04 times the complete fusion value. The close proximity of this number to the limiting complete fusion value suggests that the associated distribution of compound nucleus excitation energies is very narrow. From incomplete fusion logic, the average excitation energy is found to be 169.1±1.6 MeV and thus this data set is well matched to the $E/A=6.8$ MeV ^{64}Ni+^{100}Mo reaction which has an excitation energy of 170.4 MeV. To the extent that there is no incomplete fusion in the oxygen induced reactions and to which the compound nuclei spin distributions associated with evaporation residue formation are limited by fission competition (Sec. III A 1), then the spin distributions for the two entrance channels will also match. However, the consequences of incomplete fusion are not clear, it may further limit the spin distribution in the oxygen induced reaction (see later).

2. Charged particle emission

Energy spectra of charged particles (from rings 8 and 9) detected in coincidence with evaporation residues were again constructed. No attempt was made to extract absolute differ-

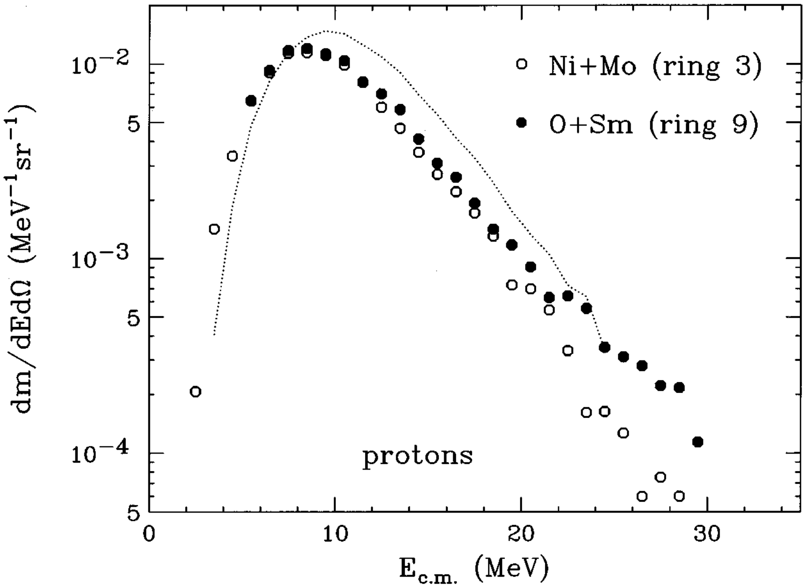

FIG. 17. Comparision of the proton energy spectra measured in the ^{16}O+^{148}Sm and the $E/A=6.8$ MeV ^{64}Ni+^{100}Mo reactions. The predictions of the statistical model calculations are indicated by the dotted curve.

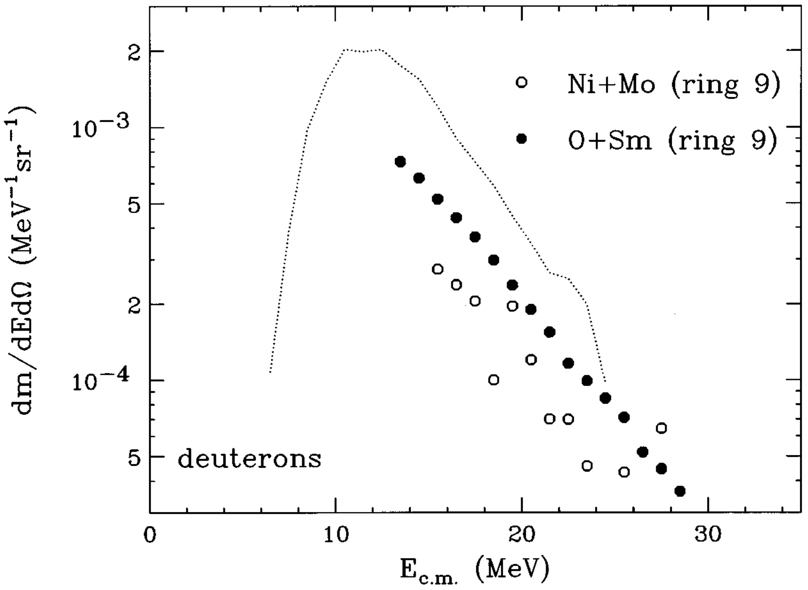

FIG. 18. Comparision of the deuteron energy spectra measured in the $^{16}O+^{148}Sm$ and the $E/A=6.8$ MeV $^{64}Ni+^{100}Mo$ reactions. The predictions of the statistical model calculations are indicated by the dotted curve.

ential multiplicities as the inclusive yield of evaporation residues is expected to be associated with events of lower average momentum transfer than those selected by the requirement of coincident charge particles in rings 8 and 9. Rather, all differential multiplicities were scaled so that the value for protons reproduced the corresponding result obtained in the $E/A=6.8$ MeV $^{64}Ni+^{100}Mo$ reaction. The resulting spectra for protons obtained from ring 9 are plotted in Fig. 17 (solid symbols). The data obtained from ring 8 are essentially identical. For comparison, the corresponding spectrum obtained with ring 3 from the matching Ni+Mo reaction is indicated by the open symbols. The shapes of the proton spectra from the matched reactions agree well with each other. The largest differences are for $E_{c.m.}>20$ MeV where a nonstatistical tail is evident for the oxygen induced reaction. Both experimental spectra are in disagreement with the GEMINI predictions indicated by the dotted curve.

For the heavier hydrogen isotopes, again only the high energy tails of the spectra are above the low-energy threshold. As with the corresponding Ni+Mo data, these exponential tails are much harder than the GEMINI predictions as illustrated in Fig. 18 for deuterons. It is therefore likely that the detected deuterons and tritons are predominately nonstatistical. The magnitude of the differential multiplicities (normalized relative to protons) shown in Fig. 18 is larger at backward angles for the lighter projectile. However, it is not surprising that this nonstatistical component is entrance-channel dependent.

The emission of α particles also shows an entrance-channel dependence, but unlike the deuterons and tritons this dependence is not clearly associated with a nonstatistical component. To illustrate this entrance-channel effect, let us first concentrate on the shape of the energy spectra as these are little affected by the bias induced by the PPAC acceptance. In order to convince the reader that the differences in the energy spectra are of greater magnitude than the experimental uncertainties, the spectra are plotted as shaded bands in Fig. 19. These bands span the maximum and minimum

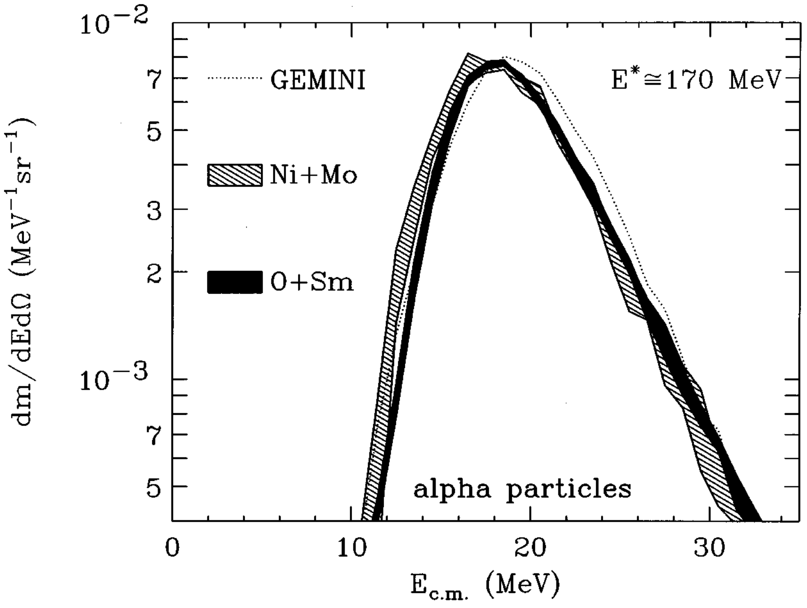

FIG. 19. Comparision of the α particle energy spectra measured in the $^{16}O+^{148}Sm$ and the $E/A=6.8$ MeV $^{64}Ni+^{100}Mo$ reactions. The predictions of the statistical model calculations are indicated by the dotted curve.

values of the relative differential multiplicities (normalized to same area) obtained from rings 2–5 and 8,9 for the Ni+Mo and O+Sm reactions, respectively. The bands therefore represent the uncertainty due to both the statistical and systematic errors. For the O+Sm reaction, the uncertainty in the compound nucleus velocity also contributes to a small uncertainty in the determination of the emitted α particle energy. Therefore spectra transformed with compound nucleus velocities of 0.94 and 1.00 times the complete fusion value (Sec. III B 1) were included when constructing the band for the O+Sm reaction.

The entrance-channel dependence of the shape of the energy spectra is small in Fig. 19. The spectrum obtained with the Ni+Mo reaction has a larger yield for the lowest α particle energies. While the slopes of the exponential tails are similar for the two experimental spectra, both of these spectra peak at lower energies than the GEMINI prediction which is indicated by the dotted curve.

In comparing the ratio of α particle to proton yields, ring 9 will be used as the average α particle emission angles are very similar, i.e., $\langle \theta_{\mathrm{c.m.}} \rangle = 162°$ and 167° for the oxygen- and nickel-induced reactions, respectively. The measured ratio of α particle to proton differential multiplicities are 0.91 ± 0.07 and 0.99 ± 0.07, respectively. However, these results are associated with different biases due to the PPAC acceptance. Using the GEMINI simulations to correct for this effect, the unbiased ratio of α particle to proton yields at these backward angles is $21 \pm 9\%$ lower in the O+Sm reaction as compared to the Ni+Mo reaction.

Both the small differences between the α particle energy spectra and between the backward relative yields indicate that there is an entrance-channel dependence in the decay of these systems. However, it is by no means clear that this is related to the effect of fusion dynamics on the decay process and/or a violation of the Bohr independence hypothesis. Although the compound nuclei excitation energies obtained in the reactions are well matched, it is not certain that this is true for the initial spin distributions. The α particle angular distributions are strongly dependent on the initial spin distribution (Sec. III A 4), and the lower relative α particle yield measured at the backward angle in the O+Sm reaction may indicate that the initial compound nucleus spin distribution is limited to lower values. In complete fusion reactions, the maximum ℓ waves associated with evaporation residues are limited by statistical fission competition (Sec. III A 1). However, in the O+Sm reaction, incomplete fusion processes may be relatively more prevalent at these large ℓ waves giving rise to compound nuclei of reduced spin.

IV. DISCUSSION

The standard statistical model calculations did not satisfactorily reproduce the experimental charged-particle data presented in the previous section. Although the data were compared with predictions from the code GEMINI, similar results and conclusions were obtained with the code EVAP [35].

For both the protons and α particles, the peak in the energy spectra is predicted to occur at larger energies than observed experimentally. This disagreement has been noted in a number of other studies [2,4–8] and is often attributed to a reduction in the Coulomb barrier. However, it is not at all clear that the mechanism responsible for this disagreement is the same for both protons and α particles. For instance, the shift between the experimental and predicted peak positions show little dependence on the bombarding energy for protons. Whereas for α particles, there is no shift at the lowest bombarding energy and it steadily grows as the bombarding energy increases. Also the predicted magnitude of the exponential tails is approximately correct for α particles, whereas they are overpredicted by ~50% for protons.

One feature of the proton and α particle spectra which is well reproduced in the statistical model simulations is the slope of the exponential tails. This feature is related to the choice of level density parameter and indicates that the experimental data are consistent with Lestone's temperature-dependent parametrization [22] used in the GEMINI calculations. In this parametrization, the level density parameter decreases from $A/8.7$ to $A/9.8$ MeV^{-1} as the excitation energy increases from 100 to 280 MeV. Both the magnitude and the temperature dependence affect the predicted slope. For example, if a temperature-independent value is assumed, then the slightly lower value of $A/11$ MeV^{-1} is needed to obtain the same results for the $E/A = 9.0$ MeV reaction. This temperature-independent value is consistent with other values extracted from slightly lower mass systems at large excitation energies [36,37].

Gonin *et al.* [4] have subtracted α particle spectra measured at $E/A \sim 9$ and 11 MeV in the ^{60}Ni+^{100}Mo reactions. The resulting ''quasi-first-chance emission'' spectrum was found to be consistent with a lower level density parameter of $A/13.8$ MeV^{-1}. This subtraction procedure was attempted in this work, but the results obtained from the different Microball rings were not consistent. It is likely that the experimental bias associated with the PPAC acceptance (which is different at different bombarding energies) causes the failure of this procedure.

The role of fusion dynamics is not clearly defined by this work. The evaporation of charged particles during the period before the fusion-induced collective modes (deformation or compression-extension) are fully damped, is expected to influence the average Coulomb barrier and decay rates. These collective modes are expected to be dependent on the entrance-channel mass asymmetry and therefore lead to a violation of the Bohr independence hypothesis. No entrance-channel dependence of the shape of the proton energy spectra was observed for $E^* \sim 170$ MeV. This is not surprising as large deformations are necessary to substantially change the average proton Coulomb barrier [5]. Futhermore, a significant fraction of the low-energy protons are emitted very late in the decay after the dominant neutron evaporation channel drives the system to the neutron-deficient region. As such, proton emission is less affected by fusion dynamics during the early stage of the decay.

A small entrance-channel effect was observed for the α particles, however, it is not clear whether this is due to a violation of the Bohr independence hypothesis or due to a mismatch in the compound nucleus spin distributions. Low-energy α particle emission was enhanced in the more symmetric Ni+Mo reaction, consistent with fusion models which predict that the more symmetric entrance channels lead to systems with larger initial deformations [12], and hence have lower average Coulomb barriers. On the other hand, the incomplete fusion process may deplete the population of compound nuclei at the highest spins in the oxygen-induced reaction. If this is the case, the emission of the lowest-energy α particles is clearly more important at these high spins. To add to the confusion, it should be noted that at higher excitation energies ($\sim$300 MeV) no entrance-channel dependence of the shape of the α particle spectra was observed for similar reactions covering a wider range of entrance-channel mass asymmetry [8]. Note also the lack of an effect for the more limited range of asymmetries in Ref. [6] for $E^* = 194$ MeV.

At lower excitation energies ($E^* \sim 50$ MeV) for the same set of reactions studied in this work, the ratio of deuteron and triton to proton yields were found to be dependent on the entrance-channel mass asymmetry [12]. It was not possible to confirm whether this effect is present at the higher excitation energy energies encountered in this work, due to the presence of the strong nonstatistical component in the deuteron and triton spectra.

Another important result of this work, is the overprediction of the multiplicities for hydrogen isotopes. Although the deuterons and tritons contain a significant nonstatistical contribution, the magnitude of the statistical component is at least a factor of 2 smaller than the statistical model predictions (Sec. III A 3). For protons, only the yield of the very lowest kinetic energies are correctly predicted ($E_{\mathrm{c.m.}} < 6$ MeV) and these are predominantly emitted at the very lowest excitation energies ($E^* < 30$ MeV) as discussed above. As the more energetically ‘‘expensive’’ deuteron and triton emissions occur only at the highest excitation energies, one may generalize and infer that the emission probability of all hydrogen isotopes is overpredicted in the statistical model for excitation energies greater than $\sim$30 MeV. The suppression of proton emissions from all but the lowest excitation energies, changes the ratio of high- to low-energy protons, and so accounts for the shift in the peak position between the measured and predicted energy spectra. The mechanism associated with this reduction in emission probabilities for hydrogen isotopes is not clear, especially since the magnitude of the α particle multiplicity is correctly predicted.

In the neighboring ^{160}Yb compound system formed with the very similar ${}^{60}\mathrm{Ni} + {}^{100}\mathrm{Mo}$ ($E/A \sim 9$ and 11 MeV) reaction, Gonin *et al.* [4] also report lower experimental charged particles multiplicities than predicted by statistical model codes. However, it is difficult to fully reconcile these results with those of this work for the same range of excitation energies ($E^* = 251$–293 MeV). For one thing, the experimental proton multiplicities reported by Gonin *et al.* for the more neutron-deficient ^{160}Yb system, are actually smaller than that obtained in this work. Futhermore, in this work the α particle multiplicity is in agreement with expectations, whereas the value reported by Gonin *et al.* is a factor of $\sim$3 less than statistical model predictions. It is difficult to envision how such a large difference in the decay properties could occur with the addition of four neutrons to the projectile.

In an attempt to further understand the results obtained in this work, we have explored, with mixed success, three mechanisms which might account for some of the discrepancies between the experimental data and the model predictions. These are discussed in the following sections.

A. Temperature dependence of the symmetry energy

Consideration was given to the effect of a predicted increase in the symmetry energy associated with the temperature dependence of effective nucleon mass in the surface of the nucleus [38]. The kinetic part of the symmetry energy is related to the level spacing at the Fermi surface and so it is also related to the level density parameter $[a(T)]$. The following temperature-dependent term was therefore included when calculating binding energies in the GEMINI simulations:

$$E_{\mathrm{sym}}^{\mathrm{kin}}(T) = \frac{\pi}{12}\left(\frac{1}{a(T)} - \frac{1}{a(0)}\right)(N-Z)^2. \tag{2}$$

The increase in the symmetry energy at the larger temperatures, drives the β valley of stability closer to $N = Z$ and so enhances neutron and reduces proton emission. However, taking $a(T)$ from Ref. [22], the magnitude of the effect was very small. For the $E/A = 9.0$ MeV Ni+Mo reaction, the predicted proton multiplicity decreases by only 5% and the tritons increase by 7%. The effect for tritons is of course in the wrong direction to reproduce the experimental data. Unless the temperature dependence of $E_{\mathrm{sym}}^{\mathrm{kin}}(T)$ is much larger and some extra mechanism is invoked to reduce the triton probability (see the next section), this effect is of little importance in understanding the data.

B. Deuteron and triton breakup

In a previous work, we have shown that a significant reduction in the predicted deuteron and triton multiplicities could be obtained [39] by using transmission coefficients calculated with the direct-reaction approach to fusion (DRAF) method [40]. In the DRAF method, the optical model imaginary potential is subdivided into an inner fusion part and an outer direct-reaction part. Transmission coefficients for fusion are calculated as the fraction of the incoming flux which is absorbed by the fusion part of the imaginary potential. The DRAF transmission coefficients are not purely barrier penetration probabilities, but contain information about the competition between fusion and direct reaction channels. For example, at large kinetic energies where the barrier penetration factor is unity, the DRAF transmission coefficients in the $d + {}^{93}\mathrm{Nb}$ system [39] approach a value closer to one half. The other $\sim$50% of the flux is associated with absorption by the direct-reaction channels.

Before using DRAF transmission coefficients one must first consider the relevance of the competition of fusion and direct reactions to the inverse evaporation process. To this end it is important to note that the bulk of the direct reaction channels involve the breakup of the deuteron due to its interaction with the target’s Coulomb field [41]. Given the high probability of such an interaction for trajectories which can lead to fusion, it is not unreasonable to infer that there is also a large breakup probability for the inverse evaporation process. Therefore the DRAF transmission coefficients must be interpreted as containing barrier penetration and approximate breakup probabilities.

There is at present no experimental deuteron-fusion or triton-fusion cross sections to constrain DRAF calculations for the mass region of interest in this work. A breakup probability of 50% or greater would be consistent with upper limits obtained in this work for the statistical components. However, protons produced in the breakup of these fragments would further exacerbate the disagreement between experimental and calculated proton multiplicities. Therefore, independent of the magnitude of the deuteron and triton breakup probabilities, some other mechanism(s) must be invoked for a full description of the emission probabilities for hydrogen isotopes.

C. Emission of ^{5}He

One possible mechanism which may contribute to some of the low-energy α particles observed at the higher bombarding energies is the emission of particle unstable states which sequentially decay producing α particles. The most likely candidate for this scenario is ground-state ^{5}He emission. There are a number reasons why α particles produced from the decay of ^{5}He fragments will enhance the low-energy region of the energy spectra. Firstly, ^{5}He has a more diffuse neutron density distribution compared to the rather compact α particle configuration. Consequentially the nuclear potential (between it and the emitting system) will have a larger radius and hence the height of the Coulomb barrier will be reduced. Futhermore when the ^{5}He nucleus decays, the resulting α particle retains, on average, only 80% of the ^{5}He kinetic energy and if this α particle is emitted backwards from the decaying ^{5}He fragment its energy will be even smaller.

The separation energy for the removal of a ^{5}He fragment is significantly larger than that for an α particle, i.e., 7.7 MeV compared to -2.7 MeV for decay from ^{164}Yb. Therefore, the emission probability is only significant at the larger excitation energies. This large separation energy is partially compensated by the reduced Coulomb barrier, as already noted, and a larger spin (3/2 $\hbar$ for ^{5}He compared to zero for α particles) resulting in a spin-weighting factor $(2s+1)$ which favors ^{5}He emission by a factor of 4. Also because of it's larger spin and greater mass, the evaporation of a ^{5}He fragment can remove more angular momentum from the decaying system. This increases the ^{5}He emission probability at the higher compound nucleus spins where the level density has a strong angular momentum dependence.

To obtain quantitative estimates of the influence ^{5}He emission, the computer code GEMINI was modified to include this decay mode and treat its subsequent breakup. In calculating the total decay width for ^{5}He emission and the distribution of the relative α-n kinetic energy in the second step, the Hauser-Feshback formalism was extended to include an integral over the line shape associated with this resonance (width$=$0.6 MeV). The line shape was taken to be that of an isolated resonance in the R-matrix formalism [42] with parameters taken from Ref. [43]. As for all other decays, a quantum treatment was used to choose the emission angles of both steps. The second step is assumed to be p-wave decay.

Transmission coefficients were calculated with the incoming-wave boundary-condition approximation using appropriate Coulomb and centrifugal potential. However, the choice of the nuclear potential introduces the largest uncertainty into the final calculations. As a first guess, the nuclear potential was taken from a global optical model analysis of ^{6}Li elastic scattering [44]. This procedure is justified for the neighboring nuclei ^{6}He, where elastic scattering data can be reproduced with ^{6}Li optical model parameters [45,46]. The Coulomb barrier determined from this nuclear potential is 2 MeV lower than the value used for α particle emission (18 MeV). However, the Coulomb barrier for ^{5}He emission might be even lower than this as ^{5}He is predicted to be spatially even more extended than ^{6}He. In Ref. [47], ^{5}He is predicted to have an rms neutron radius of 3.0 fm compared to the value 2.6 fm predicted for ^{6}He. With this in mind, a second set of transmission coefficients was calculated with the diffuseness of the nuclear potential increased by 30%. The resulting Coulomb barrier is decreased by an additional 2 MeV. Calculations with the two sets of transmission coefficients should therefore provide a reasonable range for the expected magnitude of ^{5}He emission and its influence on the α particle's energy spectrum.

Before comparing the calculations to the data, it is important to note that the short lifetime of the ^{5}He fragment has been neglected and it is assumed to decay outside of the influence of the Coulomb field of the decaying system. This is not entirely correct; the ^{5}He fragment is predicted to decay at a distance of ~ 35 fm, on average, from the center of the emitting nucleus. This distance is large enough that our separation of the emission and subsequent decay steps is meaningful, but it will lead to an underprediction of the α particle energy: The α particle has a higher Z/A ratio than ^{5}He and hence experiences a larger acceleration by the Coulomb field. Decay in the presence of the Coulomb field therefore leads to larger α particle and smaller neutron energies than are simulated in the GEMINI calculations. The magnitude of this effect is ~ 1 MeV, on average, for the α particles, which is similar in magnitude to our uncertainty in the Coulomb barrier. Also interactions of the ^{5}He fragment with the Coulomb field may decrease its lifetime and further increase the α particle energy. Therefore we have not tried to incorporate this effect into the calculations at this time.

The predicted α particle energy spectra obtained with the two sets of transmission coefficients are indicated by the dotted and dashed curves in Fig. 11. The dashed curves are associated with the lower ^{5}He Coulomb barrier and, as a consequence, it produces the larger effect. At the lowest bombarding energy, the predicted ^{5}He multiplicity is negligible and the calculated energy spectrum is essentially unaffected by the inclusion of ^{5}He emission. However, the ^{5}He multiplicity is predicted to increase rapidly with excitation energy, and the inclusion of ^{5}He emission substantially improves the agreement between the simulations and data at the higher energies. In fact, the calculations with the lower Coulomb barrier are in very good agreement with the data at all bombarding energies and at the two highest bombarding energies, these calculations predict that ^{5}He emission accounts for $\sim$30% of the α particles.

The large recoil motions associated with ^{5}He emission increases the predicted width of the evaporation residue angular distributions. The simulated angular distributions, indicated by the dashed curves in Fig. 1 for the calculations with lower ^{5}He Coulomb barrier, are also in better agreement with the experimental data. The charged-particle multiplicities obtained with the same calculations are indicated by the dashed curves in Fig. 5. The multiplicities of hydrogen isotopes are essentially unaffected by the inclusion of ^{5}He emission and the α particle multiplicities are increased slightly, but still consistent with the experiment values.

The inclusion of ^{5}He emission, therefore improves the agreement between the simulations and the experimental data. This is true for both the energy spectra of α particles and for the evaporation residue angular distributions. The largest uncertainty in predicting the ^{5}He multiplicity is associated with the choice of the Coulomb barrier. However, the calculations presented in this section, which cover a reasonable range of values for this quantity, indicate that ^{5}He emission can account for a significant fraction of the enhancement in the low-energy portion of the α particle energy spectrum and thus contributes to the apparent decrease in the Coulomb barrier.

The predicted ^{5}He emission probability shows a small dependence on the compound nucleus spin. To investigate the effect of reducing the maximum spin in the O+Sm reaction, let us concentrate on the calculation with the lower Coulomb barrier. In Fig. 11, 19% of the α particles originate from ^{5}He decay for $E/A=6.8$ MeV Ni+Mo reaction. This value is averaged over the compound nucleus spin distribution. To estimate the largest possible effect, let us assume for the O+Sm reaction that we are limited to spin zero systems. In that case, the fraction of α particles originating from ^{5}He decay drops to 14%. This change in probability with spin is too small to account for the observed entrance-channel dependence of the α particle's energy spectra and suggests there is still room for fusion dynamics to play some role in explaining this effect. However, it is important to experimentally investigate the magnitude of ^{5}He emission, before any quantitative conclusions regarding modifications to the Coulomb barrier due to deformation of other dynamical effects can be made. In any case, this indicates that α particles might not be the best probe of such effects at the higher bombarding energies.

The effect of other particle-unstable fragments was also considered. The emission of the 2^+, first excited state of ^{6}He will also give rise to low-energy α particles, however, the GEMINI calculations suggest that the multiplicity of this fragment is insignificant, $\sim$100 times less than the value for ^{5}He at $E^*=258$ MeV. The evaporation of ground-state ^{5}Li is expected to be more probable, its yield at $E^*=258$ MeV is predicted to be a factor of $\sim$6 lower than the ^{5}He yield. However, the kinetic energies of α particles produced from the decay of these fragments will not be as low as those from ^{5}He decay due to the larger Coulomb barrier for ^{5}Li evaporation. Therefore, ^{5}Li emission does not contribute to the enhancement of lowest-energy α particles.

The emission of ^{5}He fragments has been observed to accompany the spontaneous fission of ^{252}Cf [48] and the α particles produced from the decay of these fragments account for $\sim$11% of the long-range α particles which are detected in coincidence with the fission fragments. It is interesting to note that for these long-range α particles, there is also an apparent enhancement in the low-energy region of their energy spectra which has been attributed to the contribution from these ^{5}He α particles [49].

V. CONCLUSIONS

The angular distributions and energy spectra of charged particles detected in coincidence with evaporation residues has been measured for ^{64}Ni+^{100}Mo and ^{16}O+^{148}Sm reactions which produce compound nuclei with excitation energy from 100 to 280 MeV. Standard statistical model calculations incorporating only the evaporation of stable light particles were not able to reproduce the shape and magnitude of energy spectra for all charged particles. For deuterons and tritons, the energy spectra show large nonstatistical components, even for the lowest bombarding energy ($E/A=5.0$ MeV) and only upper limits could be deduced for the magnitude of the statistical component. Nevertheless, these upper limits are significantly lower than statistical model estimates. For protons and α particles, the predicted position of the peak in the energy spectra was shifted up in energy relative to experiment data. The total proton multiplicities were also overpredicted in the calculations.

Oxygen- and nickel-induced reactions were matched to produce $E^*=170$ MeV compound nuclei. The resulting proton energy spectra were found, within the experimental uncertainties, to have identical shapes apart from the presence of a nonstatistical component. However, the α particle spectra were found to display a small entrance-channel effect; the spectrum for the more symmetric reactions extends down to lower kinetic energies. The interpretation of this result is not obvious, as it is not clear how well the initial compound nucleus spin distributions were matched for the two entrance channels given our lack of understanding of the incomplete fusion processes which contributes to residue production in the O+Sm reaction.

Although the apparent decrease in α particle emission barriers may indicate that fusion dynamics affect the deexcitation process, it was shown that a significant fraction of this decrease could be accounted for within the statistical model by including the emission of ^{5}He nuclei. Statistical calculations indicated that the sequential decay of this fragment enhances the low-energy portion of the α particle spectra and at the highest excitation energies ($E^*=280$ MeV) up to 30% of the α particles may originate from such decays. However, the emission of ^{5}He fragments is unable to account for the observed entrance-channel dependence of the α particle's energy spectra and suggests there is still room for fusion dynamics to play some role in explaining the energy spectra.

A full understanding of the decay of the highly excited compound nuclei produced in this work is not obtained. The mechanism responsible for the overprediction of the emission probabilities for hydrogen isotopes is not known. Experiments are needed to determine the magnitude of ^{5}He emission and to systematically search for entrance-channel effects as a function of excitation energy. We have questioned the sensitivity of both proton and α particles as probes for the effects of fusion dynamics on the deexcitation process. It would be useful to establish whether deuterons and tritons are any better. Clearly one needs to determine whether at the backward angles, nonstatistical components are diminished and whether sequential decays from particle-unstable fragments are significant. Preliminary calculations suggest that the production of deuterons and tritons from the excited states in ^{6,7}Li is negligible for the range of excitation energies studied in this work.

ACKNOWLEDGMENTS

This work was supported by the Director, Office of High Energy and Nuclear Physics, Nuclear Physics Division of the U.S. Department of Energy under Contract Nos. DE-FG02-87ER-40316 and DE-FG02-88ER-40406.

---

[1] G. La Rana, D. J. Moses, W. E. Parker, M. Kapla, D. Logan, R. Lacey, J. M. Alexander, and R. J. Welberry, Phys. Rev. C **35**, 373 (1987).

[2] R. Lacey, N. N. Ajitanand, J. M. Alexander, D. M. de Castro Rizzo, P. Deyound, M. Kaplan, L. Kowalski, G. La Rana, D. Logan, D. J. Moses, W. E. Parker, G. F. Peaslee, and L. C. Vaz, Phys. Lett. B **191**, 253 (1987).

[3] G. La Rana, R. Moro, A. Brondi, P. Cuzzocrea, A. D'Onofrio, E. Perillo, M. Romano, F. Terrasi, E. Vardaci, and H. Dumont, Phys. Rev. C **37**, 1920 (1988).

[4] M. Gonin, L. Cooke, K. Hagel, Y. Lou, J. B. Natowitz, R. P. Schmitt, S. Shlomo, B. Srivastava, W. Turmel, H. Utsunomiya, R. Wada, G. Nardelli, G. Nebbia, G. Viesti, R. Zanon, B. Fornal, G. Prete, K. Niita, S. Hannuschke, P. Gonthier, and B. Wilkins, Phys. Rev. C **42**, 2125 (1990).

[5] M. Kildir, G. La Rana, R. Moro, A. Brondi, A. D'Onofrio, E. Perillo, V. Roca, M. Romano, F. Terrasi, G. Nebbia, G. Viesti, and G. Prete, Phys. Rev. C **46**, 2264 (1992).

[6] J. Boger, J. M. Alexander, R. A. Lacey, and A. Narayanan, Phys. Rev. C **49**, 1587 (1994).

[7] B. J. Fineman, K.-T. Brinkmann, A. L. Caraley, N. Gan, R. L. McGrath, and J. Velkovska, Phys. Rev. C **50**, 1991 (1994).

[8] M. Cinausero, G. Prete, D. Fabris, G. Nebbia, G. Viesti, G. X. Dai, K. Hagel, J. Li, Y. You, J. B. Natowitz, D. Utley, R. Wada, N. Gelli, F. Lucarelli, and M. Colonna, Phys. Lett. B **383**, 372 (1996).

[9] J. R. Huizenga, A. N. Behkami, I. M. Govil, W. U. Schröder, and J. T$\bar{\text{o}}$ke, Phys. Rev. C **40**, 668 (1989).

[10] N. G. Nicolis and D. G. Sarantites, Phys. Rev. C **40**, 2422 (1989).

[11] H. Feldmeier, Rep. Prog. Phys. **50**, 915 (1987).

[12] M. Korolija, R. J. Charity, N. G. Nicolis, D. G. Sarantites, and L. G. Sobotka, Phys. Rev. C **52**, 3074 (1995).

[13] K. Pomorski, J. Bartel, J. Richert, and K. Dietrich, Nucl. Phys. **A605**, 87 (1996).

[14] M. Thoennessen, J. R. Beene, F. E. Bertrand, C. Baktash, M. Halbert, D. J. Horen, D. G. Sarantites, W. Spang, and D. W. Stracener, Phys. Rev. Lett. **70**, 4055 (1993).

[15] K. A. Hanold, D. Bazin, M. F. Mohar, L. G. Moretto, D. J. Morrissey, N. A. Orr, B. M. Sherrill, J. A. Winger, G. J. Wozniak, and S. J. Yennello, Phys. Rev. C **52**, 1462 (1995).

[16] J. L. Barreto, N. G. Nicolis, D. G. Sarantites, R. J. Charity, L. G. Sobotka, D. W. Stracener, D. C. Hensley, J. R. Beene, C. Baktash, M. L. Halbert, and M. Thoennessen, Phys. Rev. C **48**, 2881 (1993).

[17] N. G. Nicolis and D. G. Sarantites, Phys. Rev. C **48**, 2895 (1993).

[18] D. G. Sarantites, P.-F. Hua, M. Devlin, L. G. Sobotka, J. Elson, J. T. Hood, D. R. LaFosse, J. E. Sarantites, and M. R. Maier, Nucl. Instrum. Methods Phys. Res. A **381**, 418 (1996).

[19] Janni, At. Data Nucl. Data Tables **27**, 147 (1982).

[20] R. J. Charity, M. A. McMahan, G. J. Wozniak, R. J. McDonald, L. G. Moretto, D. G. Sarantites, L. G. Sobotka, G. Guarino, A. Pantaleo, L. Fiore, A. Gobbi, and K. D. Hildenbrand, Nucl. Phys. **A483**, 371 (1988).

[21] R. J. Charity, Computer code GEMINI (unpublished). This code is available via anonymous FTP from WUNMR.WUSTL.EDU in directory /pub/gemini.

[22] J. P. Lestone, Phys. Rev. C **52**, 1118 (1995).

[23] A. V. Ignatyuk, G. N. Smirenkin, and A. S. Tishin, Yad. Phys. **21**, 485 (1975) [Sov. J. Nucl. Phys. **21**, 255 (1975)].

[24] J. M. Alexander, M. T. Magda, and S. Landowne, Phys. Rev. C **42**, 1092 (1990).

[25] D. Wilmore and P. E. Hodgson, Nucl. Phys. **55**, 673 (1964).

[26] F. G. Perey, Phys. Rev. **131**, 745 (1963).

[27] C. M. Perey and F. G. Perey, Phys. Rev. **132**, 755 (1963).

[28] F. D. Becchetti, Jr. and G. W. Greenlees, in *Polarization Phenomena in Nuclear Reactions*, edited by H. H. Barschall and W. Haeberli (University of Wisconsin Press, Madison, 1971); C. M. Perey and F. G. Perey, At. Data Nucl. Data Tables **17**, 1 (1976).

[29] L. McFadden and G. R. Satchler, Nucl. Phys. **84**, 177 (1966).

[30] K. Shima, N. Kuno, and M. Yamanouchi, Phys. Rev. A **40**, 3557 (1989).

[31] J. F. Ziegler, J. P. Biersack, and U. Littmark, *The Stopping Power and Ranges of Ions in Matter* (Pergamon, London, 1985), Vols. 1 and 2.

[32] C. K. Cline, T. E. Pierce, K. H. Purser, and M. Blann, Phys. Rev. **180**, 450 (1969).

[33] K. E. Rehm, H. Esbensen, J. Gehring, B. Glagola, D. Henderson, W. Kutschera, M. Paul, F. Soramel, and A. H. Wuosmaa, Phys. Lett. B **317**, 31 (1993).

[34] A. J. Sierk, Phys. Rev. C **33**, 2039 (1986).

[35] N. G. Nicolis, D. G. Sarantites, and J. R. Beene, computer code EVAP (unpublished).

[36] R. Wada, D. Fabris, K. Hagel, G. Nebbia, Y. Lou, M. Gonin, J. B. Natowitz, R. Billerey, B. Cheynis, A. Demeyer, D. Drain, D. Guinet, C. Pastor, L. Vagneron, K. Zaid, J. Alarja, A. Giorni, D. Heuer, C. Morand, B. Viano, C. Mazur, C. Ngô, S. Leray, R. Lucas, M. Ribrag, and E. Tomasi, Phys. Rev. C **39**, 497 (1989).

[37] A. Chbihi, L. G. Sobotka, N. G. Nicolis, D. G. Sarantites, D. W. Stracener, Z. Majka, D. C. Hensley, J. R. Beene, and M. L. Halbert, Phys. Rev. C **43**, 666 (1991).

[38] P. Donati, P. M. Pizzochero, P. F. Bortignon, and R. A. Broglia, Phys. Rev. Lett. **72**, 2835 (1994).

[39] N. G. Nicolis, D. G. Sarantites, L. G. Sobotka, and R. J. Charity, Phys. Rev. C **45**, 2393 (1992).

[40] T. Udagawa, B. T. Kim, and T. Tamura, Phys. Rev. C **32**, 124 (1985); B. T. Kim, T. Udagawa, and T. Tamura, *ibid.* **33**, 370 (1986).

[41] M. G. Mustafa, T. Tamura, and T. Udagawa, Phys. Rev. C **35**, 2077 (1987).

[42] A. M. Lane and R. G. Thomas, Rev. Mod. Phys. **30**, 257 (1958).

[43] Th. Stammbach and R. L. Walters, Nucl. Phys. **A180**, 225 (1972).

[44] L. T. Chua, F. D. Becchetti, J. Jäecke, and F. L. Milder, Nucl. Phys. **A273**, 243 (1976).

[45] R. J. Smith, J. J. Kolata, K. Lamkin, A. Morsad, K. Ashktorab, F. D. Becchetti, J. A. Brown, J. W. Janecke, W. Z. Liu, and D. A. Roberts, Phys. Rev. C **43**, 761 (1991).

[46] R. E. Warner, F. D. Becchetti, J. W. Jänecke, D. A. Roberts, D. Butts, C. L. Carpenter, J. M. Fetter, A. Muthukrishnan, J. J. Kolata, K. Lamkin, M. Belbot, M. Zahar, A. Galonsky, K. Ieki, and P. Zecher, Phys. Rev. C **51**, 178 (1995).

[47] B. S. Pudliner, V. R. Pandharipande, J. Carlson, and R. B. Wiringa, Phys. Rev. Lett. **74**, 4396 (1995).

[48] E. Cheifetz, B. Eylon, E. Fraenkel, and A. Gavron, Phys. Rev. Lett. **29**, 805 (1972).

[49] C. Wagemans, *The Nuclear Fission Process* (CRC, Boca Raton, 1991), Chap. 12.